J. Webster (ed.), *Wiley Encyclopedia of Electrical and Electronics Engineering*

HYSTERESIS AND COUPLING LOSSES IN SUPERCONDUCTORS

A key issue for most applications of superconductivity involves ac losses. Designers need to understand the mechanisms of ac losses in order to lay out the conductors and windings correctly and to predict the performance range in operation. In devices operating at the grid frequency (transformers, current limiters, generators, motors, and power transmission cables) ac losses mostly affect the cryogenic load and hence the overall efficiency of the application. In large pulsed windings [fusion magnets, (SMEs)] the coupling current loss affects the stability, that is, the ability of the superconductor to withstand magnetic field transients. The dc magnetization of a superconductor, which leads to hysteresis loss, is a crucial issue in applications such as imaging and accelerator magnets, where the residual, low field magnetization of the superconductor affects the quality (linearity and homogeneity) of the generated magnetic field.

In normal conducting materials, both dc and ac losses are due to the finite electrical conductivity. At first glance, it appears contradictory that ac losses can occur in a superconducting material, with zero electrical resistivity.

The nonreversible magnetization behavior of bulk superconductors was known well before a practical superconducting wire was manufactured; afterward, it was called "ac loss," which sounds much more negative than "magnetization loop." For single-core wires and tapes, the only ac loss was the hysteresis loss, with the associated disruptive flux jumps. For multifilamentary composites, a new source of loss (filamentary coupling loss) was identified and stimulated the development of very sophisticated strand layouts, with high resistivity barriers and mixed matrices; on the other hand, flux jumps were no longer an issue. Later on, with large stranded conductors, the biggest concern was cable loss (interstrand coupling loss): the effort to limit ac losses was focused on the cable layout rather than the internal structure of the multifilamentary composite.

Because of ac losses, the competitiveness of superconductors has been limited in many fields of applied electrical engineering. Most of the superconducting coils in use today (commercial and research) are operated in dc mode, with limited ac loss occurring during the slow charging up. In those coils, the fastest field change is seen during a safety discharge, when concern about heating or even quenching the conductor is small.

Both hysteresis and coupling current losses occur in a time-varying magnetic field, but their relative weights depend on the specific application. In power transmission cables, the hysteresis loss is by far the largest source, as well as in small, slow rate, potted windings. In large cabled conductors for big SMES and fusion poloidal field coils, the coupling current loss dominates. The hysteresis loss per unit volume is a function of the filament size. The coupling current loss per unit volume increases with the conductor size: with few exceptions, the larger the conductor, the bigger the weight of the coupling current loss.

The physical mechanism of ac losses in superconductors is no longer the object of baseline research. Most R&D activities are devoted to developing low loss, stable conductors. For design purposes, the ability to accurately calculate (i.e. predict) the ac loss during operation is crucial for a reliable and cost-effective engineering approach.

2 HYSTERESIS AND COUPLING LOSSES IN SUPERCONDUCTORS

Hysteresis Loss

In type I superconductors—for example, pure metals with defect-free lattices—the magnetic field does not penetrate the bulk of the material and the superconducting shielding currents flow only at the surface. Such materials have reversible magnetization and no hysteresis loss, with $B = 0$ and $M = -_0 H$ (Meissner effect) inside the material.

In type II superconducting materials used for practical applications, both low and high T_c, the surface shielding currents have a marginal role for the magnetization and the flux penetrates the bulk of the conductor. The nonreversible magnetization of type II superconductors is the reason for the hysteresis loss (1 2 3). The energy loss per unit volume of superconducting material, Q, can be written in a general form for a closed cycle of applied magnetic field B (e.g., an oscillation at grid frequency, a charge–discharge cycle of a magnet, or the superposition of an ac field on the background field)

$$Q = \oint M(B)\, dB \qquad (\mathrm{J/m^3}) \qquad (1)$$

where M is the average value of the magnetization inside the superconductor. The explicit expression for the local magnetization, needed to evaluate the integral, depends on the superconductor geometry and on the model selected to describe the magnetic flux penetration and the flux profiles inside the superconductor.

The formulas quoted below are for cylindrical superconducting filaments of diameter D: whenever the real cross section of the filaments is not round (e.g., oval, dendritic, or hollow filaments or clusters of bridged filaments), the parameter D in the formulas should be considered as an equivalent diameter. For tapes and flattened filaments with high aspect ratio (e.g., for some high T_c conductors), the formulas for an infinite slab can be used as a convenient approximation.

The Magnetization Curve. A dc magnetization curve for a type II superconductor is shown in Fig. 1. After cooldown, at zero field, $M = 0$. As an external magnetic field is initially applied, the shielding currents at the filament surface prevent the flux penetration into the bulk superconductor. The diamagnetism is perfect (i.e., $M = -_0 H$) as long as the applied field does not exceed the first critical field, B_{c1}. In a type II superconductor, total flux exclusion (the Meissner effect) occurs only at the beginning of the first, *virgin* magnetization: if the superconductor is cooled down in the presence of a magnetic field, no flux exclusion occurs.

Above B_{c1}, the average magnetization increases until the flux penetrates to the center of the filament, at $B = B_{p1}$. As the field increases, the diamagnetism decreases (upper branch of the curve) and the magnetization eventually becomes 0 at the upper critical field, $B = B_{c2}$ (not shown in Fig. 1). When the field is decreased, the flux profiles reverse their gradient in the filament and the average magnetization is >0 (lower branch of the curve). At $B = 0$, the flux trapped in the filaments is called *residual magnetization*.

The magnetic flux enters the filament as discrete flux quanta. The diffusion of the flux quanta in the bulk type II superconductor is restrained by the *pinning centers*, which establish field gradients (flux profiles) inside the filaments. The pinning centers are microscopic normal zones (e.g., metallurgical or lattice defects) that provide a potential hole to trap the flux quantum. According to the critical state model, a supercurrent encircles each pinning center: the strength of the pinning centers (i.e., their ability to hold the flux quanta) is a function of the fraction of the external field to the critical field, $b = B/B_{c2}$ (T, ϵ) where ϵ is the mechanical strain. Strong pinning centers are able to store large density of magnetic energy. The magnetization current density J_c is directly proportional to the volumetric density of the pinning forces in the superconductor.

The penetration field B_p is the field difference between the filament surface and the electrical center line (see Fig. 2): in Bean's model (4), J_c is assumed constant inside the filaments for a given b, and B_p is a linear function of the critical current density. For a round superconducting filament of diameter D, the penetration field B_p (b), in perpendicular and parallel orientation, is proportional to the density of the magnetization

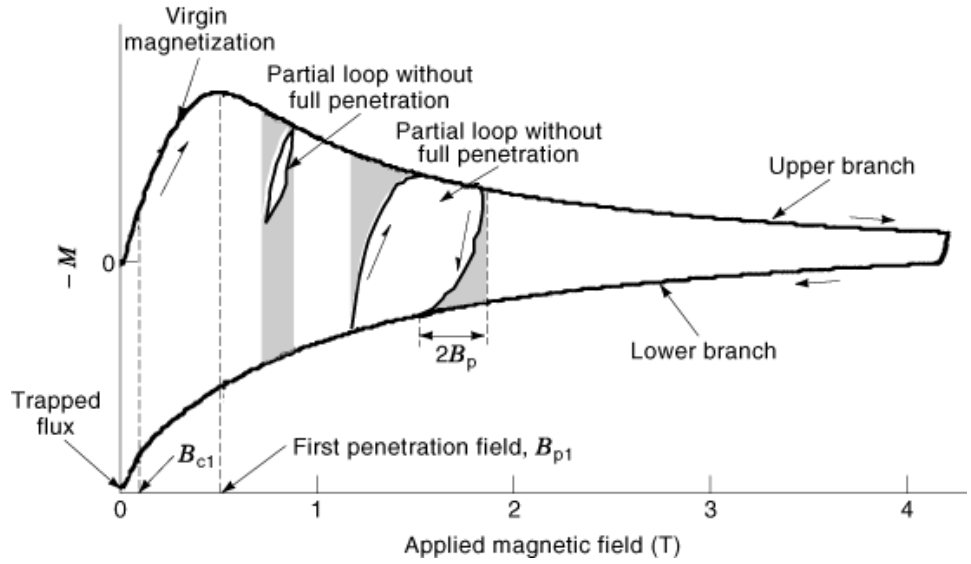

Fig. 1. Typical magnetization loop of a type II superconductor and related terminology.

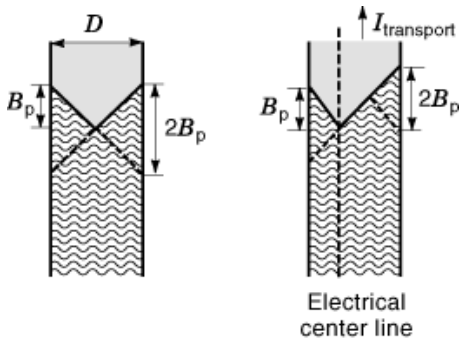

Fig. 2. Penetration field in a superconducting cylinder of diameter D in parallel applied field (or infinite slab of thickness D), without (left) and with (right) transport current. The dashed profile models the lower branch of the magnetization curve.

currents flowing respectively in the axial ($J_{c\parallel}$) and the azimuthal ($J_{c\phi}$) direction (5, 6)

$$B_{p\perp}(b) = \frac{\mu_0 D J_{c\parallel}(b)}{\pi} \quad \text{(T)}, \qquad B_{p\parallel}(b) = \frac{\mu_0 D J_{c\phi}(b)}{2} \quad \text{(T)} \qquad (2)$$

For an infinite slab of thickness $2a$, with applied field parallel to the slab surface, the penetration field is

$$B_p(b) = \mu_0 a J_c(b) \qquad \text{(T)} \qquad (3)$$

A partial magnetization loop occurs when a small external field variation is superimposed on a background dc field. If the amplitude of the field change, ΔB, is larger than $2B_p$, full penetration is achieved, that is, the magnetization moves from the upper to the lower branch of the curve.

It is questionable how far Bean's model for linear flux profiles is an acceptable approximation. When the penetration field is much smaller than the applied field, $B_p \ll B$, the J_c variation over B_p can reasonably be neglected. As B_p is proportional to the filament size, the range of field over which Bean's model reliably applies is larger for thin-filament superconductors. Whenever Bean's model is not considered adequate, an explicit formula for $J_c(b)$, such as the expression proposed by 7

$$J_c(b) = \frac{\alpha}{B_0 + b} \tag{4}$$

must be substituted in Eqs. (2) and (3) (B_0 and α are fitting parameters). The magnetization and loss formulas become more complex using Eq. (4, but the improvement in the accuracy of the loss results is not dramatic. At very low field, when the linear profile approximation is rough, the parameters in Eq. (4) cannot be satisfactorily fitted by experimental results, as a direct measurement of I_c close to 0 field is impossible due to the self-field and instabilities. The formulas below apply only to the linear profile assumption. An example of hysteresis loss formulas using a nonlinear profile approach can be found in 8.

Integrating in cylindrical coordinates the linear flux profiles from Eqs. (2) and (3) over the filament volume, the upper and lower branches of the magnetization curve are obtained as explicit functions of the critical current density and filament diameter. In perpendicular and parallel applied field orientations the average magnetization per unit volume, according to 6, is

$$M_\perp(b) = \frac{2DJ_{c\parallel}(b)}{3\pi} \quad (\mathrm{T}), \qquad M_{||}(b) = \frac{DJ_{c\phi}(b)}{6} \quad (\mathrm{T}) \tag{5}$$

Basic Formulas for Hysteresis Loss. Substituting Eq. (5) into Eq. (1), the hysteresis loss for a closed field cycle of amplitude $\Delta B = B^a - B^b$ is obtained as a function of the average critical current density or the average penetration field, defined by

$$\bar{J}_{c\parallel} = \frac{\int_{B^a}^{B^b} J_{c\parallel}(B)\,dB}{B^b - B^a}, \quad \bar{B}_{p\perp} = \frac{\int_{B^a}^{B^b} B_{p\perp}(B)\,dB}{B^b - B^a} \tag{6a}$$

and

$$\bar{J}_{c\phi} = \frac{\int_{B^a}^{B^b} J_{c\phi}(B)\,dB}{B^b - B^a}, \quad \bar{B}_{p\parallel} = \frac{\int_{B^a}^{B^b} B_{p\parallel}(B)\,dB}{B^b - B^a} \tag{6b}$$

The results of the integration are summarized in Table 1 for the three cases of an infinite slab of thickness $2a$ with field parallel to the slab surface and a cylinder with diameter D perpendicular and parallel to the applied field. The formulas are different for partial penetration ($\Delta B \le 2B_p$) and full penetration ($\Delta B \ge 2B_p$). A further, easier formula is proposed for $\Delta B \gg 2B_p$: this formula overestimates the loss. The shaded areas in (Fig. 1) give a measure of the excess, which is accounted for by using the formula reported in Table 1 for $\Delta B \gg 2B_p$.

For a given ΔB, the loss maximum occurs when $\Delta B = 2B_p$. The loss maximum, Q_{max}, reported in Table 1, is a fraction of the magnetic field energy density; it does not depend on the critical current, critical temperature, strain, or filament diameter. In some cases, it may be useful to use Q_{max} to get a feeling for the worst-case loss

Table 1. Summary of Hysteresis Loss [a] Formulae

	Infinite Slab Parallel to Field	Cylinder Parallel to Field	Cylinder Perpendicular to Field
$\Delta B \le 2B_p$	$\frac{\Delta B^3}{12\mu_0 B_p}$	$\frac{\Delta B^3}{3\mu_0^2 D J_{c\phi}}\left(1-\frac{\Delta B}{2\mu_0 D J_{c\phi}}\right)$ $=\frac{\Delta B^3}{6\mu_0 B_{p\parallel}}\left(1-\frac{\Delta B}{4B_{p\parallel}}\right)$	$\frac{\pi\Delta B^3}{3\mu_0^2 D J_{c\parallel}}\left(1-\frac{\pi\Delta B}{4\mu_0 D J_{c\parallel}}\right)$ $=\frac{\Delta B^3}{3\mu_0 B_{p\perp}}\left(1-\frac{\Delta B}{4B_{p\perp}}\right)$
$\Delta B \ge 2B_p$	$\frac{\Delta B B_p}{\mu_0}\left(1-\frac{4B_p}{3\Delta B}\right)$	$\frac{\Delta B D\bar{J}_{c\phi}}{3}\left(1-\frac{\mu_0 D(J^{\perp}_{c\phi}+J^{\parallel}_{c\phi})}{4\Delta B}\right)$ $=\frac{2\Delta B\,\bar{B}_{p\parallel}}{3\mu_0}\left(1-\frac{B^{\perp}_{p\parallel}+B^{\parallel}_{p\parallel}}{2\Delta B}\right)$	$\frac{4\Delta B D\bar{J}_{c\parallel}}{3\pi}\left(1-\frac{\mu_0 D(J^{\perp}_{c\parallel}+J^{\parallel}_{c\parallel})}{2\pi\Delta B}\right)$ $=\frac{4\Delta B\,\bar{B}_{p\perp}}{3\mu_0}\left(1-\frac{B^{\perp}_{p\perp}+B^{\parallel}_{p\perp}}{2\Delta B}\right)$
$\Delta B \gg 2B_p$	$\frac{\Delta B B_p}{\mu_0}$	$\frac{\Delta B}{3}D\bar{J}_{c\phi}=\frac{2\Delta B}{3\mu_0}\bar{B}_{p\parallel}$	$\frac{4\Delta B}{3\pi}D\bar{J}_{c\parallel}=\frac{4\Delta B}{3\mu_0}\bar{B}_{p\perp}$
Q_{max} at $\Delta B = 2B_p$	$\frac{\Delta B^2}{6\mu_0}$	$\frac{\Delta B^2}{6\mu_0}$	$\frac{\Delta B^2}{3\mu_0}$

[a] As energy per unit volume of superconductor, Q, for a closed cycle of magnetic field ΔB.

without performing time-consuming calculations. For a given ΔB, the filament parameters J_c and D determine the reduced field b for which $\Delta B = 2B_p(b)$ is fulfilled, that is, the loss is maximum (9). The loss formulas in Table 1 may also be written as a fraction of Q_{max} or of the magnetic field energy density $\Delta B^2/2_0$, thus introducing a dimensionless loss factor, which is, for a given geometry, only a function of $\Delta B/B_p(b)$ (10). In Table 1, Q is the hysteresis loss per unit filament volume and J_c is the filamentary critical current density. For some superconducting strands, such as Nb_3Sn and high T_c superconductors, the noncopper critical current is referred to instead of the filamentary critical current density. Whenever the exact filament fraction is not known, it is possible to use the loss formulas for $\Delta B \gg 2B_p$, replacing J_c by the noncopper critical current I_c. The hysteresis loss is then expressed in joules per meter of conductor length.

Anisotropy and Variable Angle Orientation. Due to the integration path of the flux profiles in the axial and radial direction of the cylindrical filament, the ratio of the magnetization in parallel and perpendicular field orientation is, according to Eq. (5),

$$\frac{M_\parallel}{M_\perp} = \frac{4J_{c\phi}}{\pi J_{c\parallel}} \tag{7}$$

The difference observed in the amplitude of magnetization measurements at 0° and 90° orientation is larger than $4/\pi$ and reveals of the anisotropy of the critical current density, that is, $J_{c\phi} \neq J_{c\parallel}$.

In NbTi filaments, the largest source of pinning centers is the precipitation of α-Ti and cell dislocation (11). During the manufacturing process (drawing and annealing), the pinning centers are created and strongly oriented in the axial direction. The pinning forces are very anisotropic, resulting in a critical current density much larger in the azimuthal direction than in the axial direction. The ratio $J_{c\phi}/J_{c\parallel}$ in NbTi conductors is a function of the field and also depends on the manufacturing history (filament size, alloy composition, cold work): from experimental magnetization measurements, the critical current anisotropy is $J_{c\phi}/J_{c\parallel} \approx 3$ (12).

In Nb_3Sn conductors, the major source of pinning centers is the grain boundaries that form during the reaction heat treatment. The anisotropy of the critical current density is linked to the grain orientation, which

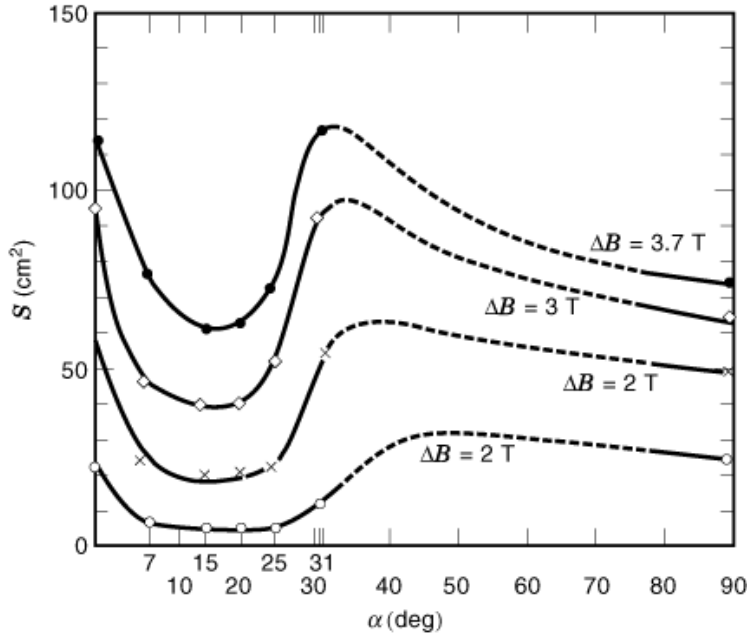

Fig. 3. Areas of the magnetization loops versus the orientation angle between filaments and applied field. Single core NbTi strand, $D = 127$ m. From 6. Reprinted from *Cryogenics*, **18**, A. P. Martinelli and B. Turck, Some effects of field orientation on the magnetization of superconducting wires, pp. 155–161, copyright 1978, with permission from Elsevier Science.

is influenced by the heat treatment schedule. The Sn diffuses radially into the Nb filaments, and the Nb_3 grains are elongated in the radial direction, giving a higher density of the boundary lines for the axial critical current (13). Typical values of the anisotropy in filamentary Nb_3 are $J_{c\phi}/J_{c\|} \approx 0.5$ (14).

The anisotropy of the critical current density should not be confused with the variation of the transport critical current as a function of the orientation angle α of the applied field, $J_c(B_\alpha)$. The azimuthal critical current density, $J_{c\phi}$, to be used for the hysteresis loss in parallel field orientation, is not the same as the transport critical current measured with parallel field orientation, $J_{c\phi} \neq J_c(B_\|)$, but $J_{c\|} \equiv J_c\,(B_\perp)$. For both NbTi and Nb_3 Sn conductors, a larger transport current has been observed in the parallel applied field, $J_c\,(B_\|) > J_c\,(B_\perp)$ (6, 14,15,16).

The orientation of the superconducting filaments in cabled conductors with respect to the cable axis changes continuously over a broad range of angles. For large, multistage conductors, average strand angles of 16° to 25° are commonly observed: the range of the strand angles and its statistical distribution depend on the number of cable stages and the pitch sequence. The hysteresis loss at intermediate angles cannot be interpolated from the formulas in parallel (0°) and perpendicular (90°) fields. The behavior of the loss as a function of the angle has been observed to be not monotonic, with a peak around 30° and a minimum at small angle (<10°); see Fig. 3 from 6. The interference of the magnetization currents flowing in longitudinal and azimuthal directions distorts the flux profiles and does not allow a practical definition of the penetration field. At angles close to 0°, the flux profiles adjust themselves for consecutive field cycles and the loop area decreases until a reproducible magnetization is obtained after 10 to 20 cycles. An attempt to model the magnetization at intermediate angles can be found in 17.

Filament Diameter. The filament diameter is a key parameter for the hysteresis loss formulas. It can be either estimated directly from metallographic examination of the strand cross section or deduced from the magnetization and critical current measurements.

For most of the commercial NbTi strands, the magnetization currents are confined to the individual filaments: permanent currents linking groups of filaments by proximity effects are observed only in very thin, highly packed filaments, with submicron interfilament spacing (11). The critical field for proximity effects, B_{c1p}, is a function of the temperature, transport current, ratio of spacing to filament size, matrix resistivity and impurities, twist pitch, and sample length (18,19,20).

For A15 superconductors, as well as for high-temperature superconductors, the estimation of the filament diameter from metallographic investigation is not accurate. In the Nb_3Sn strands, because of different access to the Sn source (for both bronze method and internal Sn strands), the filaments do not all grow to the same size. A nonreacted Nb core may be left in some region of the filamentary zone, turning the Nb_3Sn cylinders into hollow cylinders. A major problem affecting the assessment of the filament diameter in Nb_3 composites is *bridging*: when the Nb filaments are tightly packed in the matrix, the Nb_3Sn layers grow during the reaction heat treatment to build either continuous superconducting links between filaments (21) or mechanical contacts (22), which behave like the proximity effects. The density of bridging is a function of the spacing to filament ratio *s/d* (or local area ratio between Cu–CuSn matrix and Nb filaments) and of the heat treatment schedule (23). The superconducting properties of the bridges linking the filaments may be different from those of the bulk filament: at higher field, temperature, or strain, some of the links may become too weak for the magnetization currents. In these cases, the filament diameter is a function of b. The paths of the magnetization currents in a cluster of randomly bridged filaments cannot be analytically modeled: whenever bridging occurs and the loss formulas for cylinders are used, the equivalent filament diameter must be determined from the magnetization curve, preferably at different b.

Three main methods are used to derive the filament diameter from the magnetization measurement in a perpendicular field. All methods use Bean's model and assume that the filament critical current density is directly measured in the same field range. The same methods can also be applied to deduce the critical current density once the filament diameter is known (e.g., to estimate $J_{c\phi}$ or the low field $J_{c\|}$, when a direct measurement of I_c is not possible).

- *Diameter from the Penetration Field*. The minimum field change to move from the upper to the lower branch of the magnetization curve (see Figs. 1 and 2) is $\Delta B_p = 2B_p$. The filament diameter can be estimated using Eq. (2) or (3) and $\Delta B_p(B)$ from the magnetization curve. The advantage of this method is that no calibration of the magnetization is necessary to estimate ΔB_p.
- *Diameter from the Amplitude of the Magnetization*. The filament diameter can be deduced using Eq. (5) from the amplitude of the magnetization, measured as half of the distance from the lower to the upper branch of the curve. The accuracy of this method is limited by the calibration of the magnetization.
- *Diameter from the Energy Loss of a Closed Field Cycle*. The hysteresis energy loss for a closed field cycle (magnetization loop) can be estimated either by the line integral of the magnetization curve, according to Eq. 1, or by the calorimetric method, after subtracting the coupling loss contribution, if any. If the calorimetric method is used, the magnetization does not need to be calibrated. According to the amplitude of the applied field ΔB ($B_{p\perp} > \Delta B$ or $B_{p\perp} < \Delta B$), the measured energy is compared with the formulas in Table 1 to deduce the filament diameter.

Crossing the Zero Field. The formulas for magnetization and hysteresis loss have limited validity at low applied fields, especially at the zero-field crossing. On one side, the linear flux profile approximation (Bean's model) is very rough at fields smaller than the first penetration field, and below B_{c1} the surface screening currents prevent any flux change inside the filament. On the other hand, non-current-carrying superconducting materials are sometimes included for manufacturing reasons in technical superconducting strands, resulting in low field perturbations of the magnetization curve. In soldered cables, the low field superconductivity of the solder may also play a similar role.

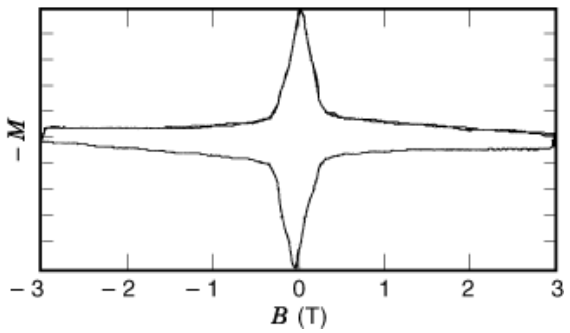

Fig. 4. Magnetization loop of a Nb_3Sn multifilamentary strand with Nb + Ta diffusion barrier. The low field peak of the magnetization is due to the pure Nb shell with diameter ≈0.5 mm.

In thin filament NbTi strands, a Nb shell encircles each filament to prevent TiCu intermetallic formation during the intermediate heat treatment process, and some Nb_3Sn suppliers use a Nb layer as diffusion barrier or include it to buffer the Ta or V barrier on the side facing the stabilizer. In both cases, a continuous Nb shell is left on the outer side of the barrier. When a continuous Nb_3Sn ring grows from the Nb diffusion barrier, its magnetization is as much as one order of magnitude larger than that in the filament (24).

The pure Nb behaves like a *soft* type II superconductor, with $B_c \approx 0.18$ T. The effect of the screening currents in the Nb layer on the outer side of the diffusion barrier, whose diameter is more than 100 times larger than that of the filament, can be clearly recognized as a low field peak in the magnetization curve; see Fig. 4.

Whenever an anomaly of the magnetization curve occurs at the zero crossing, large errors are likely in the hysteresis loss calculation. If the filament diameter is derived from microscopic examinations or from the higher field magnetization, the loss at low field will be substantially underestimated by the loss formulas. In contrast, if the energy loss of a bipolar field cycle is used to deduce the filament diameter, this, and hence the higher field loss, will be overestimated, because of the additional contribution of the Nb below 0.18 T. The range of the operating conditions should dictate the decision on the criterion to be used for the filament diameter. If necessary, a correction factor can be added in the calculation code to include the Nb magnetization contribution at the zero-crossing field.

Hysteresis Loss with DC Transport Current. When a longitudinal current is superimposed on the transverse field magnetization currents of a filament, the electrical center line is moved to the periphery of the filament (or slab), the flux profiles are asymmetric, and the penetration field decreases by a factor $1 - i$, where i is the ratio of the longitudinal current (also called the *transport* current) to the critical current

$$i = \frac{I_{\mathrm{tr}}}{I_{\mathrm{c}\parallel}(b)}, \qquad B^i_{\mathrm{p}\perp} = B_{\mathrm{p}\perp}(1 - i) \quad (\mathrm{T}) \tag{8}$$

Below penetration (i.e., for $\Delta B < 2B^i{}_{\mathrm{p}\perp}$), the low ΔB amplitude formula in Table 1 can also be used in the presence of a dc transport current. Above penetration, the magnetization decreases as a function of the transport current, dropping to 0 for $i = 1$, that is, $I_{\mathrm{tr}} = I_c$. For large ΔB, the area of the magnetization loop (i.e., the energy supplied by the external field change) decreases when a transport current is superimposed on the magnetization currents [see Fig. 5(b) from 25]

$$\text{for} \quad \Delta B \gg 2B^i_{\mathrm{p}\perp}, \qquad Q^i_\perp \approx Q_\perp(1 - i^2) \quad (\mathrm{J/m^3}) \tag{9}$$

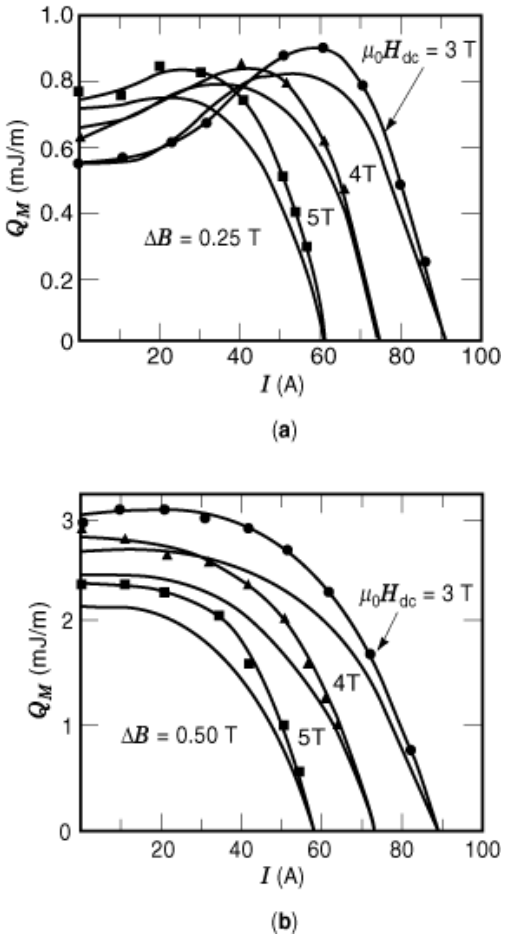

Fig. 5. Magnetization loss as a function of the dc transport current for a single core NbTi conductor: (a) $\Delta B = 0.25$ T $< 2B^{i=0}{}_{p\perp}$, (b) $\Delta B = 0.50$ T $> 2B^{i=0}{}_{p\perp}$. From 25. Reprinted from *Cryogenics*, *25*, T. Ogasawara, Y. Takahashi, K. Kanbara, Y. Kubota, K. Yasohama, and K. Yasukochi, Alternating field losses in superconducting wires carrying dc transport currents: Part 1. Single core conductors, pp. 736–740, copyright 1979, with permission from Elsevier Science.

As a function of the transport current, the magnetization loss increases until full penetration is achieved for $\Delta B = 2B_{p\perp}\ (1 - i)$. A further increase of the transport current decreases the magnetization loss; see Figs. 5(a) and 6 from 25.

A change of the filament magnetization beyond $2B^{i}{}_{p\perp}$ is opposed by the power supply, which works to maintain the transport current, that is, the asymmetric flux profiles. A voltage appears along the filament, and an extra energy Q_d due to the dynamic resistance R_d must be added to the magnetization loss (26, 27). Above penetration, the dynamic resistance is proportional to the amplitude of the field change and inversely proportional to the duration t_0 of the field change

$$\text{at} \quad \Delta B < 2B^{i}_{p\perp}, \qquad R_d = 0 \tag{10}$$

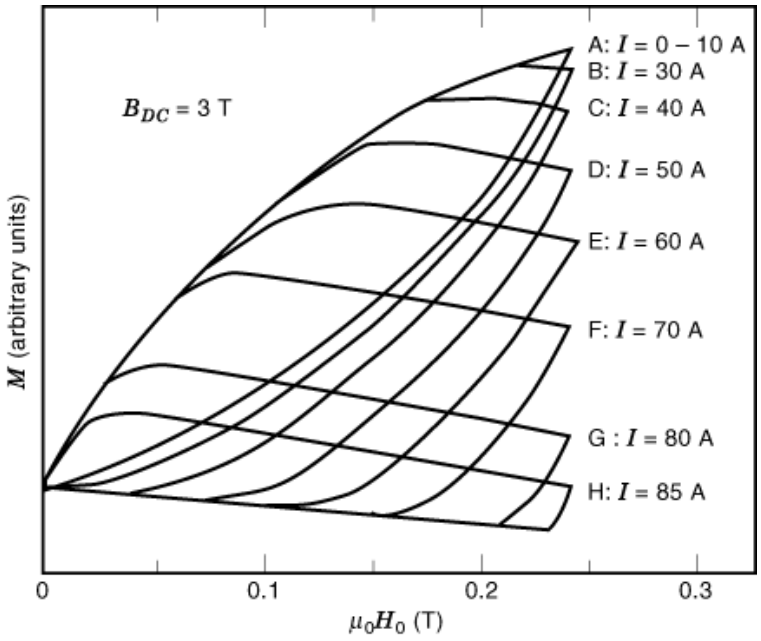

Fig. 6. Magnetization loops at increasing transport current for a single core NbTi conductor ($D = 250\ \mu$m), with $\Delta B = 0.25$ T, from 25. The magnetization loss is maximum at F, when $2B^{i=60}{}_{p\perp} = 0.25$ T; see also Fig. 5(a). Reprinted from Single core conductors, pp. 736–740, copyright 1979, with permission from Elsevier Science.

$$\text{at} \quad \Delta B > 2B^{i}_{p\perp}, \qquad R_d \propto \frac{\Delta B - 2B^{i}_{p\perp}}{t_0} \tag{11}$$

For $\Delta B \gg 2B^{i}{}_{p\perp}$, $R_d \propto \dot{B}$, that is, the energy loss per cycle, Q_d, is proportional to i^2 but is independent of the field rate. The total loss in filaments carrying a dc transport current is

$$\text{for} \qquad \Delta B \gg 2B^{i}_{p\perp}, \quad Q^{\text{total}} = Q_d + Q^{i}_{\perp}$$
$$= \quad Q_{\perp}(1 + i^2) \quad (\text{J/m}^3) \tag{12}$$

From Eq. (12), at $\Delta B \gg 2B^{i}{}_{p\perp}$ the ratio of the total loss with transport current to the magnetization loss is ≤ 2 for any transport current. For $B_{p\perp} \geq \Delta B/2 > B^{i}{}_{p\perp}$, the loss enhancement factor can be much larger than a factor of two (10). This can be understood by remembering that the low ΔB magnetization loss is proportional to ΔB^3, but the dynamic resistance loss Q_d is proportional to $\Delta B \cdot i^2$.

The transport current also affects the azimuthal magnetization currents, modifying the local field orientation angle. Some kind of dynamic resistance is also expected because of the interference of I_{tr} with $J_{c\phi}$.

Equations (9) and (12) give a satisfactory and validated (25) model for a single-core strand. However, two assumptions are required to extend them to a multifilamentary strand or to a cable of stranded wires:

- Each filament of each strand carries the same fraction of critical current.
- The longitudinal current is constant during the external field change.

Both assumptions are highly unlikely: On one hand the current distribution is not homogeneous across either the cable or the filaments of an individual strand. On the other hand, the several coupling current loops induced by a field change cause local, time-dependent, very large variations of the current density compared with the average value.

Self-Field Loss. A special case of hysteresis loss occurs for a straight, solid conductor carrying a longitudinal current in the absence of any external field. The flux penetration is due only to the self-field, which is proportional to the longitudinal current. Full penetration and maximum loss occur for $I = I_c$. For ac operation, it is convenient to write the hysteresis loss per unit length per cycle as a function of i, the ratio of the peak current to the critical current. 28 proposed a formula for self-field loss in an isolated thin slab and a round (or elliptical) filament

For round or elliptical cross section

$$q_r = \frac{I_c^2 \mu_0}{\pi}\left((1-i)\ln(1-i) + \frac{(2-i)i}{2}\right) \quad \text{(J/m)} \qquad (13)$$

For a thin slab

$$q_s = \frac{I_c^2 \mu_0}{\pi}[(1-i)\ln(1-i) + (1+i)\ln(1+i) - i^2] \quad \text{(J/m)} \qquad (14)$$

For conductors with the same critical current, the loss ratio at saturation (i.e., at $i = 1$) is $Q_r/Q_s = 1.3$. At small fractions of the critical current, $Q_r/Q_s = 1/i$, showing that the advantage of the thin slab geometry is significant only at very small current density.

In a round multifilamentary composite, the filaments are not transposed for self-field, and the filamentary zone of diameter D_{fz} can be treated as a single core, applying a filling factor λ for the critical current. 10 discusses the self-field loss for a round multifilamentary composite in terms of penetration field. The complete penetration field is $B_{ps} = {}_0\lambda J_c D_{fz}/2$, and the partial penetration field is $B_{ms} = iB_{ps}$. The loss per cycle per unit filament volume is

$$Q = \frac{B_{ms}^2}{2\mu_0}\left(\frac{2}{i} - 1 + \frac{2(1-i)}{i^2}\ln(1-i)\right) \quad \text{(J/m}^3\text{)} \qquad (15)$$

Equation (15) can be written in terms of critical current, as a loss per unit length, and becomes

$$q = \frac{\lambda I_c^2 \mu_0}{\pi}\left((1-i)\ln(1-i) + \frac{(2-i)i}{2}\right) \quad \text{(J/m)} \qquad (15a)$$

which is identical to Eq. (13) except for the filling factor λ. In the case of an oscillating, unidirectional current, i is defined as the ratio of transport to critical current, and the loss formula proposed by 10 as loss per unit length, becomes,

$$q = \frac{\lambda I_c^2 \mu_0}{\pi}\left[2(2-i)\ln\left(\frac{2-i}{2}\right) + \frac{(4-i)i}{2}\right] \quad \text{(J/m)} \qquad (16)$$

The use of thin filaments does not help to reduce the self-field loss, as the nontransposed filamentary zone behaves like a single core with critical current reduced by the filling factor λ. When the self-field loss

becomes a crucial issue, it is recommended to select a transposed cable or braid, where the filamentary zone of the individual strands is kept as small as possible.

The preceding formulas have become very popular in the high temperature superconductor community, although both Norris and Wilson warned about the limits of their applicability. The assumption of constant critical current may result in significant errors at low field. The twist in the multifilamentary composites introduces a spiral component of the self-field. For cabled conductors, the field from the neighboring strands may give rise to coupling current loss, not taken into account in the preceding formulas.

Accuracy of Hysteresis Loss Estimation. The overall accuracy of the hysteresis loss estimation is affected by the simplifications assumed in the model, the accuracy of the conductor parameters, the local field orientation, the distribution of the transport current (29, 30), and the nonfilamentary magnetization at low field. The weight of the individual error sources depends on the conductor layout and operating conditions. The use of sophisticated computer codes does not help much to improve the accuracy of the hysteresis loss prediction, which lies, in the best cases, around 20%.

Model Accuracy. The geometrical basis for hysteresis formulas is either a cylinder or an infinite slab. The actual filament geometry, especially in the case of bridging, is not a cylinder: even when an equivalent diameter is defined, it does not perfectly model the real filament over the entire range of operating conditions.

Bean's assumption of linear flux profile may be a source of inaccurate estimation of the magnetization and penetration field at low magnetic field, especially for thick filaments, strands, and tapes. In addition, the model does not account for surface screening currents below B_{c1}.

The loss formulas may include the effect of the strain and temperature on J_c and B_p, but the integration of the magnetization is done under isothermal conditions. A step-by-step integration, calculating the magnetization from the instantaneous value of J_c (T,ϵ), also would not be correct: an increase of T or $|\epsilon|$ at constant field decreases the magnetization, as J_c decreases and more flux penetrates. However, a decrease in T or $|\epsilon|$ at constant field leaves the flux profiles, and hence the magnetization, unchanged.

Coupling Current Loss

Two filaments in a strand, as well as two noninsulated strands in a cabled conductor, constitute a loop for induced currents under a perpendicular time-varying field, that is, they are *coupled* in a current loop. A large portion of the loop is superconducting, that is, the linked area is large but the loop resistance is small. To reduce the linked area, the filament bundle is twisted and the strands are cabled with tight pitches, leading to transposition with respect to the perpendicular field (31).

The magnetic energy, initially stored in the coupling current loop, is released as Joule heating by the resistive decay of the induced currents, with a time constant, τ, which is the ratio of the loop inductance to the loop resistance. In a round, ideal multifilamentary strand, with the filaments homogeneously distributed over the cross section, the time constant for the interfilament coupling currents is a function of the twist pitch l_t and the transverse resistivity ρ

$$\tau = \frac{\mu_0 l_t^2}{8\pi^2 \rho} \quad \text{(s)} \qquad (17)$$

The transverse resistivity ρ in a multifilamentary composite is a function of the bulk resistivity ρ_m, of the matrix and the superconducting fraction in the filamentary zone λ. If no resistance barrier is found at the

interface between filaments and matrix, according to 32 the transverse resistance is

$$\rho = \rho_m \frac{1-\lambda}{1+\lambda} \qquad (\Omega \cdot m) \tag{18}$$

When a high resistivity barrier builds up around the filaments (e.g., in hot extruded NbTi composites), the transverse resistance is assumed to be

$$\rho = \rho_m \frac{1+\lambda}{1-\lambda} \qquad (\Omega \cdot m) \tag{19}$$

In a cable of noninsulated strands, the interstrand coupling currents add to the interfilament loops. In a multistage cable, a large variety of coupling current loops exists, each with an individual time constant τ_i. The size of the loops depends on the length and sequence of the cable pitches, but the exact path of the coupling currents, and hence the transverse resistance, is hard to predict (33). As a general trend, the transverse resistance is larger and the loss is smaller when the pitches of the different cable stages all have the same direction (34) and their ratio is close to one, that is, short pitches are used for the higher cable stages and long pitches for the lower cable stages.

In most cases, the loss is not homogeneously distributed over the strand or cable volume: a dimensionless geometry factor, n_i, is associated with each current loop with time constant τ_i. The geometry factor (35,36,37) allows for the demagnetization effects (e.g., round versus flat conductor) and normalizes the loss to the overall strand volume (e.g., when the filament bundle is surrounded by a large normal metal shell) or to the cable volume (e.g., when an interstrand current loop is restricted to a fraction of the cable volume).

Steady State Coupling Loss Formulas. When the time scale of a field change (e.g., the duration of a linear ramp or the period of a field oscillation) is much larger than any of the conductor time constants, steady state conditions are established for the coupling currents. For linear field change, with constant dB/dt, the power loss (10, 35, 38) per unit volume of strand material is

$$P = \frac{n\tau}{\mu_0} \dot{B}^2 \qquad (W/m^3) \tag{20}$$

For sinusoidal field variations $B = (\Delta B/2 \sin \omega t$, with frequency π and $= 2\pi$, the average power loss (10, 35, 39) is

$$\bar{P} = \frac{n\tau}{8\mu_0} \Delta B^2 \, \omega^2 \qquad (W/m^3) \tag{21}$$

The energy loss Q_c for a field cycle of amplitude ΔB is respectively

$$\begin{aligned} Q_c &= \frac{2n\tau}{\mu_0} \dot{B} \, \Delta B \quad (J/cycle \cdot m^3), \\ Q_c &= \frac{\pi n \tau}{4\mu_0} \Delta B^2 \, \omega \quad (J/cycle \cdot m^3) \end{aligned} \tag{22}$$

For cabled conductors with multiple current loops and associated time constants, the $n\tau$ in the preceding formulas is the sum of the individual terms

$$n\tau = \sum_i n_i \tau_i \qquad \text{(s)} \tag{23}$$

In steady-state conditions, where all the current loops are fully activated, it is not necessary to know the breakdown of $n\tau$ into individual components. The average coupling loss can be calculated from the overall $n\tau$, obtained, for example, from measurements on a short conductor section.

The tool for experimental assessment of the coupling currents loss is the *loss curve*, where the energy per cycle per unit volume of strand (or cable) is plotted as a function of the field rate, for a linear ramp, or the frequency, for a sinusoidal field sweep. The hysteresis loss is the extrapolation of the loss curve to $dB/dt = 0$. From the initial slope of the loss curve, $n\tau$ is derived using the steady-state formulas, Eq. (22).

Transient Coupling Loss Formulas. The energy loss per unit volume in Eq. (22) is linear in the field rate or frequency. However, the energy loss has an obvious upper limit set by the magnetic field energy density, $\Delta B^2/2_0$. At $\tau > 0.3$ and at ramp time $t_0 < 10\tau$, Eqs. (20 21 22) give a loss overestimation larger than 10% and should be replaced by transient field loss formulas.

For multifilamentary strands in an oscillating field, the currents flowing in the outer filament layers screen the inner volume of the conductor. In a fast ramped field, the field penetrates the innermost layers with the time scale of the decaying screening currents τ, even if the duration of the applied field change is smaller. In fully transposed cables, the mechanism of screening depends on the interstrand current loops and is hardly predictable.

For conductors characterized by a single time constant τ, the transient formulas for sinusoidal oscillations (35), linear ramp (10), and exponential decay (40) are respectively for $B = (\Delta B/2) \sin t$,

$$\begin{aligned} \bar{P} &= \frac{n\tau\ \Delta B^2\ \omega^2}{8\mu_0(1+\omega^2\tau^2)} \qquad \text{(W/m}^3\text{)} \\ Q_c &= \frac{\pi n\tau\ \Delta B^2\ \omega}{4\mu_0(1+\omega^2\tau^2)} \qquad \text{(J/cycle} \cdot \text{m}^3\text{)} \end{aligned} \tag{24}$$

for $\dot{B} = \Delta B/t_0$

$$Q_c = \frac{\Delta B^2\ n\tau}{\mu_0 t_0}\left[1 - \frac{\tau}{t_0}\left(1 - e^{-t_0/\tau}\right)\right] \qquad \text{(J/m}^3\text{)} \tag{25}$$

$\dot{B}$ for $B = \Delta B(1 - e^{-t/t_0})$

$$Q_c = \frac{\Delta B^2\ n\tau}{2\mu_0(t_0+\tau)} \qquad \text{(J/m}^3\text{)} \tag{26}$$

In case of multiple time constants, Eqs. (24 25 26) cannot be applied using the $n\tau$ defined in Eq. (23). If each current loop behaved independently (i.e., the screening currents of the largest loops did not affect the applied field at the other loops), the total transient loss would be the sum of the individual i-contributions. From

Eqs. (24) and (25)

$$Q_c = \sum_i Q_c^i = \frac{\pi \omega \, \Delta B^2}{4\mu_0} \sum_i \frac{n_i \tau_i}{1 + \omega^2 \tau_i^2} \qquad (\mathrm{J/cycle \cdot m^3}) \quad (27)$$

$$Q_c = \sum_i Q_c^i = \frac{\Delta B^2}{\mu_0 t_0} \sum_i n_i \tau_i \left[1 - \frac{\tau_i}{t_0} \left(1 - e^{t_0/\tau_i} \right) \right] \qquad (\mathrm{J/m^3}) \quad (28)$$

On the assumption that the larger current loops screen the smaller current loops, which is what happens in nontransposed conductors, a formula for the transient loss in a sinusoidal field has been proposed in 37 for a conductor with N loops

$$Q_c = \frac{\pi}{4\mu_0} \Delta B^2 \left(\frac{\omega n_N \tau_N}{1 + \omega^2 \tau_N^2} + \sum_{k=1}^{N-i} \frac{\omega n_k \tau_k}{1 + \omega^2 \tau_k^2} \prod_{l=k+1}^{N} \frac{1}{1 + n_l \omega^2 \tau_l^2} \right) \qquad (\mathrm{J/cycle \cdot m^3}) \quad (29)$$

It is hard to reliably predict the transient coupling loss in a large multistage cable. On one hand, the overall $n\tau$ should be broken down into the individual $n_i\tau_i$: the procedure to add the $n\tau$'s measured separately on the lower cable stages is not satisfactory, as the transverse resistance and the current loops change when the subcables are bundled together. On the other hand, because the current path for each loop is not known, it is hard to decide to what extent the higher loops do screen the smaller loops, that is, to decide between Eqs. (28) and (29).

In conductors with multiple time constants, the largest underestimation of the transient field loss occurs when the Eqs. (24 25 26) for a single time constant are applied. The steady state formulas, Eqs. (20 21 22), give the largest overestimation. Whenever the breakdown of the overall $n\tau$ is known, Eqs. (27–28) give a better, but still conservative, estimate, because they assume no screening. On the contrary, Eq. (29) is rather optimistic, because it treats the current loops as nested shells. Equation (29) has been used to find the $n\tau$ components from the experimental loss curves in 37 and 41.

An example of coupling loss prediction for a conductor with multiple time constants is shown in Fig. 7. The steady-state, overall time constant is assumed to be $n\tau = 100$ ms (e.g., drawn from an experimental loss curve). The breakdown of the time constant is assumed to be $\tau_1 = 2$ ms, $\tau_2 = 8$ ms, $\tau_3 = 40$ ms, and $n_1 = n_2 = n_3 = 2$ (round cross section). The plot in Fig. 7 shows the loss according to Eqs. (22), (24), (27), and (29), for an applied field oscillation $B = (\Delta B/2)/\sin t$, with $\Delta B = 2$ T. At low frequencies (i.e., for $\tau < 0.2$), all the formulas give the same result, but at higher frequencies the assumptions about the current paths and the multiple screening lead to substantially different results.

Saturation of Coupling Currents. According to the coupling loss formulas, the energy dissipation occurs in the resistive section of the induced current loops, that is, in the composite matrix for interfilament coupling loss and at the strand-to-strand contacts for the interstrand coupling loss. At a first approximation level, the coupling currents are assumed not to change the filament magnetization. Actually, the coupling currents flowing in the outer filament layers create in steady state a field difference across the multifilamentary zone. The associated magnetization loss is referred to as *penetration loss* and can be treated in analogy to the hysteresis loss of a solid filament of the size of the filamentary zone, D_{fz}, with a critical current λJ_c, where λ

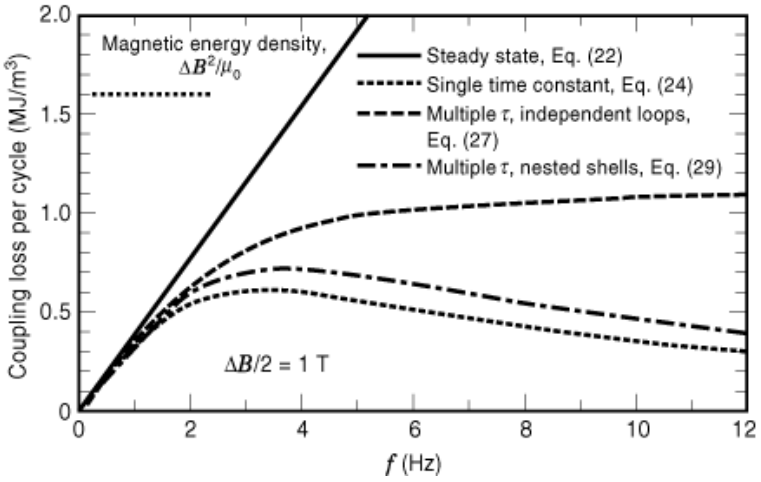

Fig. 7. Example of prediction of coupling loss in oscillating field, for a conductor with multiple time constant, $n\tau = n_1\tau_1 + n_2\ \tau_2 + n_3\ \tau_3 = 4 + 16 + 80 = 100$ ms. The plot shows the result obtained neglecting the shielding effect, Eq. (22), and with three different approaches to taking account of shielding.

is the superconductor fraction in the filamentary zone (39). In steady state, the penetration loss per cycle Q_p, normalized to the volume of the filamentary zone, can be easily found by replacing $B_{p\perp}$ by $\tau\dot{B}$ in the formulas of Table 1:

$$Q_p = \frac{4\tau\ \Delta B\ \dot{B}}{3\mu_0} \qquad (\mathrm{J/cycle \cdot m^3}) \qquad (30)$$

The total loss in a round multifilamentary composite with $n = 2$ is the sum of the coupling loss, according to Eq. (20), and the penetration loss

$$Q_{tot} = Q_c + Q_p = \frac{4\tau\ \Delta B\ \dot{B}}{\mu_0} + \frac{4\tau\ \Delta B\ \dot{B}}{3\mu_0} = \frac{16\tau\ \Delta B\ \dot{B}}{3\mu_0} \qquad (\mathrm{J/cycle \cdot m^3}) \qquad (31)$$

Whenever the loss is experimentally assessed, the penetration loss does not need to be added to the coupling loss, because it is already buried in the $n\tau$ inferred from the loss curve. The penetration loss for an oscillating field and for a transient field are discussed in 39 and 10.

At high field rates, the coupling currents may reach the critical current. The outer filament layer is saturated, and the difference between outer and inner fields is the penetration field for the filamentary zone, $\tau\dot{B} = B^{fz}{}_p = \mu_0\lambda J_c D_{fz}/\pi$. Saturation in a multifilamentary composite occurs whenever

$$\frac{\pi\tau_{str}\dot{B}}{\mu_0\lambda J_c D_{fz}} \geq 1 \qquad (32)$$

The saturation loss is the upper limit of the penetration loss and is obtained by substituting $B^{fz}{}_p$ for $\tau\dot{B}$ in Eq. (30):

$$Q_{sat} = \frac{4\ \Delta B}{3\pi} D_{fz} \lambda J_c \qquad (J/m^3) \tag{33}$$

When the condition of Eq. (32) is fulfilled (i.e., when the current loops are saturated), the coupling loss does not increase for higher field rates. The maximum total loss in a multifilamentary composite for a long duration (steady-state) field change is independent of τ and can be written by substituting Eqs. (32) and (33) into Eq. (31):

$$\begin{aligned} Q_{tot}^{max} &= Q_c + Q_{sat} = \frac{4\tau\ \Delta B}{\mu_0} \frac{\mu_0 \lambda J_c D_{fz}}{\pi \tau} + \frac{4\ \Delta B}{3\pi} D_{fz} \lambda J_c \\ &= \frac{16\ \Delta B\ \lambda J_c D_{fz}}{3\pi} \qquad (J/cycle \cdot m^3) \end{aligned} \tag{34}$$

Coupling Loss with Transport Current. As long as coupling currents and transport current use a small fraction of the superconducting cross section, the influence of the transport current is limited to the hysteresis loss change. At a higher field rate or higher i (ratio of transport current to critical current), all the superconducting cross section is eventually engaged to carry either the transport or the coupling currents. The criterion for saturation with transport current in Eq. (32) becomes

$$\frac{\pi \tau_{str} \dot{B}}{\mu_0 \lambda J_c D_{fz}} \geq 1 - i \tag{35}$$

The larger i is the smaller the loop current (and hence the field rate) is to achieve saturation. Above saturation (i.e., when $2I_{loop} + I_{transport} > I_c$), the excess of transport current must be accommodated in the superconducting cross section carrying $-I_{loop}$. The paths of the coupling currents, with the current direction reversing with the periodicity of the transposition pitch, force the transport current (or a fraction of it) to switch continuously from one to the other filament (interfilament coupling) or strand (interstrand coupling) to match $-I_{loop}$. The energy dissipated is at the expense of the power supply, and it is called the *dynamic resistance* loss (29), because of the analogy between hysteresis and coupling loss due to transport current (see 42 for a discussion of the limits of this analogy). Whenever a transport current is imposed, the magnetic energy density of the applied field cannot be considered as an upper limit for the overall loss.

Above saturation, the coupling currents (and coupling loss) decrease and the dynamic resistance loss sharply increases. The behavior of the total loss as a function of i over the full range of $\dot{B}$ has been calculated analytically for a slab; see Fig. 8 (from 29). A cylinder requires a numerical calculation for the saturation range (43), leading to a results similar to Fig. 8. Experimental results on interfilament loss with transport current (29, 43) confirm the behavior of Fig. 8. At a very large field rate (i.e., when saturation occurs even at $i = 0$), the effect of the transport current on the overall loss is an increase by a factor $1 + i^2$

$$Q_{sat}(i) = (1 + i^2) Q_{sat}(0) \qquad (J/m^3) \tag{36}$$

At an intermediate field rate (i.e., when saturation is achieved only above a certain value of transport current)

$$1 > \frac{\pi \tau_{str} \dot{B}}{\mu_0 \lambda J_c D_{fz}} > 1 - i \tag{37}$$

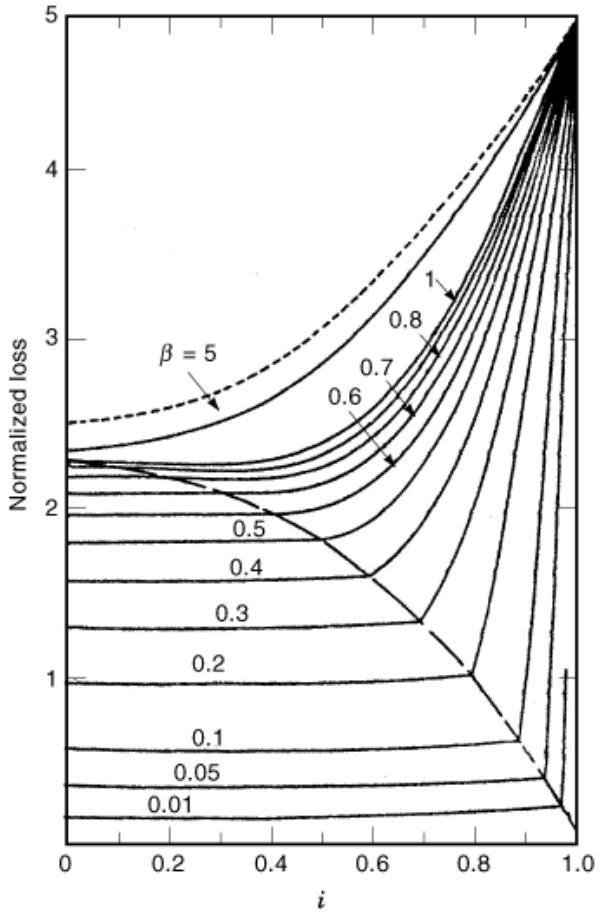

Fig. 8. Normalized loss, $Q/(\dot{B}^{fz}{}_p/_0)$, in a slab geometry as a function of the transport current fraction i for different $\beta = \tau\dot{B}/B^{fz}{}_p$ (29). The locus of the knees of the curves shows the saturation threshold. Above saturation, the loss is dominated by the dynamic resistance. Reprinted from *Cryogenics 20*, T. Osagawara, Y. Takahashi, K. Kanbara, Y. Kubota, K. Yasohama, and K. Yasukochi, Transient field losses in multifilamentary composite conductors carrying dc transport currents, pp. 216–222, copyright 1980, with permission from Elsevier Science.

the behavior of the total loss as a function of i is complex [see (29, 42, 43)]. Using $Q_c(i) = (1 + i^2)Q_c$ (0) is not recommended and may lead to large errors in the actual loss values.

In large cable-in-conduit conductors, the occurrence of saturation cannot be exactly predicted from Eq. (35). If the current loops (i.e., the coupling currents) are not homogeneously distributed, a redistribution of the transport current at the start of the field change may avoid the occurrence of saturation and dynamic resistance loss in steady state. Using Eq. (35) with the average i and the overall cable time constant is very conservative and may result in an underestimate of the field rate causing saturation. In cable in conduit with multiple time constants, where only the overall $n\tau$ is known, it may be difficult to select the correct τ to be used in Eq. (35). An example of saturation of coupling currents in a large cable-in-conduit conductor with nonhomogeneous current distribution is reported in 44.

Coupling Loss in Flat Cables. In flat cables and in rectangular composites with sides a and b, both n and τ are much larger for field perpendicular to the broad side a of the cable. The loss ratio for the

two orthogonal orientations has been calculated as a function of the aspect ratio $\alpha = a/b$ for conductors with homogeneous transverse resistivity. The results obtained by Murphy et al. with concentric ellipses (45), Turck et al. with concentric rectangles (46), and Campbell with rounded-edge concentric layers (35) are respectively

$$\frac{Q_c^{\perp a}}{Q_c^{\perp b}} = \alpha^4, \qquad \frac{Q_c^{\perp a}}{Q_c^{\perp b}} = \alpha^2 \frac{35 + 20\alpha + 7\alpha^2}{35\alpha^2 + 20\alpha + 7}, \qquad \frac{Q_c^{\perp a}}{Q_c^{\perp b}} = \frac{\alpha^4}{4} \tag{38}$$

In practical large flat cables, an insulating (or high-resistivity) strip is placed in the midplane to increase the transverse resistance of the coupling currents for field orientation perpendicular to a; see for example 47. In such cases, the 38 are no longer valid and the loss anisotropy is reduced (48).

At intermediate angles, an analytical loss formula is proposed in 45, modeling the flat cable as an ellipse with homogenous transverse resistivity. In practical, nonhomogeneous flat cables, the coupling loss for field orientation at an angle θ with respect to the broad side a can be roughly estimated by splitting the field into the orthogonal components and adding the loss contributions

$$Q_c(\theta) = Q_c^{\perp a} \sin^2 \theta + Q_c^{\perp b} \cos^2 \theta \qquad (\mathrm{J/m^3}) \qquad (39)$$

For flat cables with a large aspect ratio, the second term in Eq. (39) can be neglected over a broad range of angles.

Coupling Loss in Spatially Changing Magnetic Field. When a superconducting cable is exposed to a time-varying magnetic field that is not homogeneous along the conductor, the periodicity of the boundary conditions for the coupling currents loops is affected. If the flux linked by two geometrically identical current loops next to each other is not balanced, the coupling currents extend beyond the boundary of the pitch length. In one-stage cables (e.g., one-layer flat cables and Rutherford cables), adjacent strand pairs may build current loops with different flux balance in the presence of a spatial gradient of magnetic field. Because of the different boundary conditions, the individual strand pairs carry coupling currents of different amplitude. The inductance associated with these *extended* current loops is larger and the resistance is smaller, resulting in time constants that may be orders of magnitude larger than with strictly periodic boundary conditions. The result is a strong, quasi-steady-state current imbalance and larger loss.

49 50 first did an analysis of the coupling loss in a spatially changing magnetic field for flat cables. The subject, later named , (BICCs), assumed a much larger relevance in the context of Rutherford cables for accelerator magnets. Here, the spatial field gradients along the conductor at the saddles of the dipole magnets are large and occur over a length smaller than the cable pitch. The long-lasting current imbalance across the cable leads to field distortions (51, 52) and ramp rate limitations in the accelerator dipoles (53, 54).

The variation of the strand crossover resistance along Rutherford cables has also been shown to be a potential reason for *BICC*s (53). In multistage cable-in-conduit conductors, the current loops do not have a regular pattern, as a result of the nonhomogeneous distribution of the interstrand resistance. Flux imbalance for current loops next to each other is expected to be frequent in large cable-in-conduit conductors, even in a spatially homogeneous magnetic field.

Interstrand Resistance in Cable-in-Conduit Conductors. (CICCs) are a special case of multistage cables. What makes the *CICC*s different is the tribological nature of the transverse resistance, which is only marginally determined by the bulk properties of the metallic components. A database for coupling currents loss in *CICC*s and its implication for stability is discussed in 55.

In *CICC*s with void fraction in the range of 30% to 40%, the coupling currents may follow complex, zigzag paths through a number of good electrical contacts at the strand crossovers. Rather than the 2-D smeared transversal resistivity, the interstrand resistance is the critical parameter, together with the pitch length, for

assessing and controlling the coupling loss in *CICC*s. The interstrand resistance in *CICC*s has units of ohm-meters and is measured as the dc resistance between a strand pair embedded in a cable, multiplied by the length of the cable section, which should be longer than a pitch length. For the same conductor, the interstrand resistance in a CICC may vary as much as 20% from piece to piece and as a function of the sample length and homologous strand pair (56).

NbTi Strands. The interstrand resistance depends on the operating transverse load and on the conductor history, including contact surface oxidation, heat treatment, and cycling. In *CICC*s made of bare NbTi strands, the interstrand resistance, as well as the coupling loss, may have a broad range of results (57): the thin layer of copper oxide that develops at room temperature at the strand surface provides a precarious resistive barrier, which may either partly dissolve or break under heat treatment and/or applied load (58 59 60). The electromagnetic load in operation can also produce a dramatic increase in the coupling loss in *CICC*s made of bare NbTi strands (61, 62). Whenever long term, reliable control of the coupling loss is desirable, it is recommended to use a surface coating for the NbTi strands.

Several coatings have been investigated on NbTi strands for contact resistance, mostly in the frame of the Rutherford cable development for accelerator magnets, including Zn, SnAg, Ni, and Cr. The SnAg (Stabrite) soft coatings produce very low contact resistance with applied load (59, 63) and are not recommended for low-loss cables. A resistive barrier can be obtained by a diffusion heat treatment at 200°C of the SnAg-coated strand before cabling, building a Sn-rich bronze shell at the surface; however, the diffusion heat treatment also affects the (RRR) of a fraction of the stabilizer. The Ni coating, as well as the Zn, has higher contact resistance and is not sensitive to curing heat treatment and applied load (63). The Cr coating has proved to be effective in cutting the interstrand loss in medium-sized *CICC*s (64, 65). A direct comparison of contact resistance for bare and Cr- and Ni-plated strands indicates almost one order of magnitude higher resistance for Cr than for Ni and another order of magnitude difference between Ni and clean Cu (57).

Nb_3 Sn Strands. In *CICC*s of bare Nb_3Sn strands, diffusion bonding (sintering) occurs at a number of strand crossovers during heat treatment, resulting in low interstrand resistance and high coupling loss (66). The Cr coating has been identified as a reliable, thin coating to avoid sintering during the heat treatment, with moderate effect on the strand *RRR*.

The effect of the Cr plating on the coupling loss of Nb_3Sn-based *CICC*s has been the object of systematic investigations. A comparison of CICC samples identical except for Cr plating by vendors (67) has found a variation as high as a factor of four for the interstrand resistance (and the loss), depending solely on the proprietary electroplating processes. The influence of the Cr plating process parameters on the contact resistance is discussed in 68.

The void fraction is an important parameter affecting the interstrand resistance and coupling loss in *CICC*s, with a low loss range above 40% voids and a large loss range below 30% (69). The looseness of the cable in the jacket may play an even more important role than the average void fraction: the electromagnetic forces associated with the coupling currents tend to pull apart the strand bundle and relax the contacts at the strand crossovers.

The most striking effect observed in the interstrand resistance of Cr-plated Nb_3Sn *CICC*s is the decrease in resistance after heat treatment and the increase after mechanical (70) and/or electromagnetic loading (44, 71). The diagram in Fig. 9 shows the evolution of the interstrand resistance at different steps: the large drop after the heat treatment may be due to a partial depletion of O from the Cr oxide at the sealed surface of the strand crossovers. The subsequent increase of the interstrand resistance after bending loads (as happens in the react and transfer coil manufacturing process) or transverse loads (Lorentz forces in operation) can be understood in terms of microscopic movements of the crossovers, which partly lose their initial engagement. An important lesson learned from these results is that most loss test results obtained for short samples in the virgin state (i.e., as heat-treated, without any load) overestimate the loss by about one order of magnitude compared with the actual coil operating conditions.

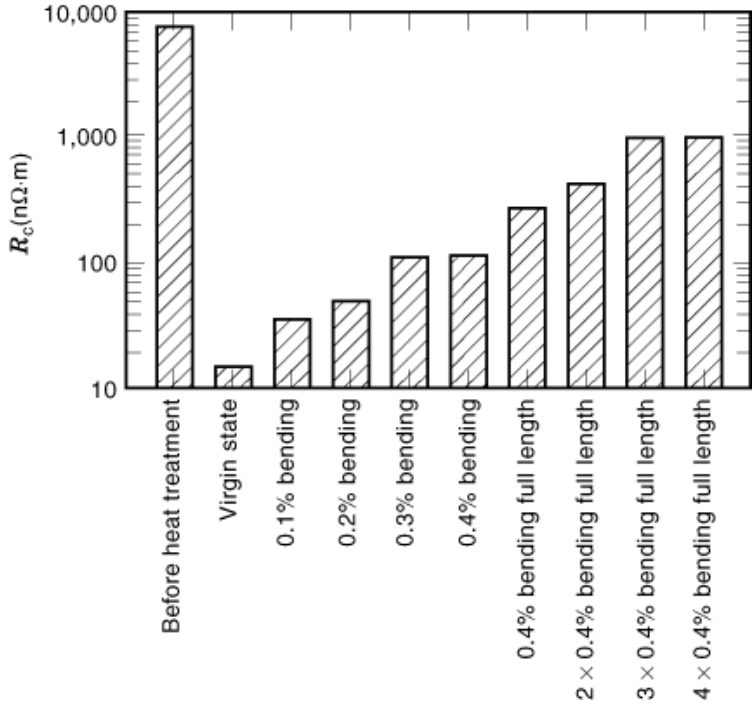

Fig. 9. Evolution of the interstrand resistance in a Cr-plated Nb_3Sn CICC (81 strands, 30%), before and after the heat treatment and after controlled bending strain.

Target Interstrand Resistance for CICCs. The goal of the designer is to obtain in operation a value of interstrand resistance large enough to reduce the coupling loss to an acceptable level but small enough to allow fast and effective current redistribution among the strands and provide stability under transient local disturbances.

The experimental results on the interstrand resistance R_c and the coupling current constant $n\tau$, measured on the same Nb_3Sn *CICC*s specimens, have been correlated in 55 to obtain

$$R_c \approx \mu_0 \frac{l_t^2}{n\tau} \qquad (\Omega \cdot \mathrm{m}) \tag{40}$$

Once the acceptable coupling loss is assessed and the cable pitch l_t is known, Eq. (40) indicates the *minimum* design value for the interstrand resistance, that is, for the kind of strand coating to be selected. The *maximum* allowable value for the interstrand resistance is assessed by the requirement on the interstrand current sharing length, l_0. According to 72

$$l_0 = \sqrt{R_c / R_\parallel} \qquad (\mathrm{m}) \tag{41}$$

where R (Ω/m) is the normal longitudinal resistance of the strand per unit length. Combining Eqs. (40) and (41), a criterion for interstrand resistance in *CICC*s summarizing the coupling loss and stability requirements

is obtained according to 55

$$\frac{\mu_0 l_t^2}{n\tau} < R_c < l_0^2 R_{\parallel} \qquad (\Omega \cdot \mathrm{m}) \qquad (42)$$

In very large *CICC*s, Eq. (42) may need a correction if the interstrand resistance for the first cable stage, to be used for the current-sharing length, is significantly smaller than in the cable stage where the largest loss occurs (73).

Accuracy of Coupling Current Loss Estimation. The calculation of the coupling current loss in steady-state conditions is based on the experimental value of $n\tau$, drawn from the loss curve. In other words, to estimate the coupling loss for a coil in operation, it is necessary to measure first the loss on a conductor specimen under controlled conditions. The assessment of $n\tau$ from the pitch and the expected transverse resistivity may lead to very rough loss estimates.

The accuracy of $n\tau$ depends on the loss calibration method, the resolution and reproducibility of the loss measurements, and the number of test points in the linear range of the loss curve ($n\tau$ is inferred by linear regression from the initial slope of the loss curve). In multistage, cabled conductors, the loss curve may show slight deviations from linearity at a very low field rate, possibly due to very large time constants associated with the very small factor n (41). In such cases, the actual operating field rate should drive the choice of the range of the loss curve from which $n\tau$ must be inferred. Typical experimental values of $n\tau$ have an error bar larger than 10% (74).

When the coupling currents are not in steady state (transient field change or high frequency oscillations), the product $n\tau$ from the loss curve must be broken down into n and τ to use the transient formulas from Eqs. (24 25 26 27 28 29). This is very hard to do, especially in the case of multiple time constants. A measurement of τ from the decay time of the induced currents is discussed in 75 for conductors with a single (or dominant) time constant.

Besides the issue of breaking down the overall $n\tau$, the prediction of non-steady-state loss in conductors with multiple time constants is made difficult by the choice between a model with independent current loops or with nested loops (see discussion of Fig. 7). For $\tau \gg 1$ or ramp time $t_0 \leq \tau$, the error in loss estimation may be large and the transient formulas should be used only to provide the order of magnitude of the expected loss.

In large cable-in-conduit conductors, the accuracy of the coupling loss estimation is much worse than in multifilamentary composites. On one hand, it is hard to reproduce in a short sample measurement the actual load history for interstrand resistance and hence to obtain a reliable result for $n\tau$ in operation. On the other hand, the nonhomogeneous distribution of the interstrand resistance may give rise, in a coil, to complex patterns of *BICC*s, not measurable on a short sample (61, 62). In the presence of a transport current, more incertitude is added because of the occurrence of dynamic resistance loss and the variation of current density across the cable (44, 73).

Concluding Remarks

Although the basic mechanisms of ac losses in superconductors are well known, the optimization of low-loss conductor design and the prediction of ac losses in operation are still the subject of several studies and much R&D activity. The complexity of the conductor layout and the variety of the boundary conditions conclusively show that the existing formulas and models need systematic improvement.

The challenging task for the designer consists in distinguishing, for an individual application, the relevant from the negligible sources of ac losses and implementing measures to reduce their effect on the overall performance of the device. Reduction of ac losses is always a welcome result, but it must be carefully balanced

with possible negative effects (e.g., reduction of the overall current density due to passive components or poor stability due to impaired current sharing).

The task of calculating ac losses may be challenging, although no complex finite-element models are required, as they are for example in thermohydraulic and mechanical analyses. For the hysteresis loss a rough estimate is easy to make, because the results for a single filament can be reliably scaled to large conductors. However, very accurate predictions are not easy.

Estimating the coupling current loss for large conductors may be difficult. The electrodynamic behavior can be predicted only on the basis of several assumptions, which can hardly be verified. Small-scale experiments, even on full-sized conductors, are mostly unable to fully reproduce the actual operating conditions.

BIBLIOGRAPHY

1. D. Saint-James E. J. Thomas, G. Sarma, *Type II Superconductivity*, New York: Pergamon, 1969.
2. A. M. Campbell J. E. Evetts, Flux vortices and transport currents in type II superconductors, *Adv. Phys.* **21** (90): 333–357, 1972.
3. H. Ullmaier, *Irreversible Properties of Type II Superconductors*, New York: Springer-Verlag, 1975.
4. C. P. Bean, Magnetization of hard superconductors, *Phys. Rev. Lett.*, **8**(6): 250–253, 1962.
5. C. Y. Pang, P. G. McLaren, A. M. Campbell, Losses in superconducting cylinders in transverse field, *Proc. ICEC*, **8**: 739–743, 1980.
6. A. P. Martinelli B. Turck, Some effects of field orientation on the magnetization of superconducting wires, *Cryogenics*, **18**: 155–161, 1978.
7. Y. B. Kim, C. F. Hempstead, A. R. Strnad, Critical persistent currents in hard superconductors, *Phys. Rev. Lett.*, **9**: 306–309, 1962.
8. H. Brechna C. Y. Hwang, Hysteretic effects in pulsed superconducting magnets, *Cryogenics*, **19**: 217–223, 1979.
9. K. Kwasnitza P. Bruzzone, Hysteresis losses of multifilament superconductors in superimposed dc and ac fields, *Cryogenics*, **21**: 593–597, 1981.
10. M. N. Wilson, *Superconducting Magnets*, London: Oxford Univ. Press, 1983.
11. E. W. Collings, *Applied Superconductivity, Metallurgy and Physics of Titanium Alloys*, New York: Plenum, 1986.
12. M. P. Mathur et al., Anisotropy of the critical current density in the NbTi filaments of round composite superconductors, *J. Appl. Phys.*, **43** (9): 3831–3833, 1973.
13. H. H. Farrell, G. H. Gilmer, M. Suenaga, Grain boundary diffusion and growth of intermetallic layers: Nb_3Sn, *J. Appl. Phys.*, **45**: 4025–4035, 1974.
14. T. Schild, J. L. Duchateau, D. Ciazynski, Influence of the field orientation on the critical current density of Nb_3 strands, *IEEE Trans. Appl. Supercond*, **7**: 1512–1515, 1997.
15. S. Takacs, M. Polak, L. Krempasky, Critical currents of NbTi tapes with differently oriented anisotropic defects, *Cryogenics*, **23**: 153–159, 1983.
16. M. Jergel S. Takacs, The dependance of critical current of Nb_3Sn tapes on the direction of a transverse magnetic field, *J. Low Temp. Phys.*, **10** (3/4): 469, 1973.
17. J. F. Artaud, Distribution de courant dans des fils supraconducteurs soumis à un champ magnétique d'orientation quelconque, PhD Thesis, Univ. de Aix-Marseille, France, 1994.
18. T. S. Kreilick, E. Gregory, J. Wong, Influence of filament spacing and matrix material on the attainment of high quality, uncoupled NbTi fine filaments, *IEEE Trans. Magn.*, **24**: 1033–1036, 1988.
19. M. Polak et al., Anomalous magnetization behavior in fine filamentary NbTi superconducting wires, *IEEE Trans. Appl. Supercond.*, **3**: 150–153, 1993.
20. M. D. Sumption E. W. Collings, Influence of twist pitch and sample length on proximity effect coupling in multifilamentary composites described in terms of a field independent, two current region model, *Cryogenics*, **34**: 491–505, 1994.
21. A. K. Gosh, K. E. Robins, W. B. Sampson, Magnetization measurements of multifilamentary Nb_3Sn and NbTi conductors, *IEEE Trans. Magn.*, **21**: 328–331, 1985.
22. R. B. Goldfarb K. Itoh, Reduction of interfilament contact loss in Nb_3 superconductor wires, *J. Appl. Phys.*, **75**: 2115–2118, 1994.

23. R. B. Goldfarb J. W. Ekin, Hysteresis losses in fine filament internal-tin superconductors, *Cryogenics*, **26**: 478–481, 1986.
24. S. S. Shen, Effect of the diffusion barrier on the magnetic properties of practical Nb_3Sn composites, *Adv. Cryog. Eng. Mat.*, **28**: 633–638, 1982.
25. T. Ogasawara et al., Alternating field losses in superconducting wires carrying dc transport currents: Part 1. Single core conductors, *Cryogenics*, **19**: 736–740, 1979.
26. T. Ogasawara et al., Effective resistance of current carrying superconducting wire in oscillating magnetic field 1: Single core composite conductor, *Cryogenics*, **16**: 33–38, 1976.
27. S. S. Shen R. E. Schwall, Interaction of transport current and transient external field in composite conductors, *IEEE Trans. Magn.*, **15**: 232–235, 1979.
28. W. T. Norris, Calculation of hysteresis losses in hard superconductors carring ac: Isolated conductors and edges of thin sheets, *J. Phys. D*, **3**: 489–507, 1970.
29. T. Ogasawara et al., Transient field losses in multifilamentary composite conductors carrying dc transport currents, *Cryogenics*, **20**: 216–222, 1980.
30. D. Ciazynski et al., Ac losses and current distribution in 40 kA NbTi and Nb_3Sn conductors for NET/ITER, *IEEE Trans. Appl. Supercond.*, **3**: 594–599, 1993.
31. M. N. Wilson et al., Experimental and theoretical studies of filamentary superconducting composites, *J. Phys. D*, **3**: 1517–1546, 1970.
32. W. J. Carr, Jr., Conductivity, permeability and dielectric constant in a multifilament superconductor, *J. Appl. Phys.*, **46** (9): 4043–4047, 1975.
33. K. Kwasnitza P. Bruzzone, Large ac losses in superconducting Nb_3Sn cable due to low transverse resistance, *Proc. ICEC11*, 741–745, Berlin, 1986.
34. K. Kwasnitza I. Horvath, Experimental evidence for an interaction effect in the coupling losses of cabled superconductors, *Cryogenics*, **23**: 9–14, 1983.
35. A. M. Campbell, A general treatment of losses in multifilamentary superconductors, *Cryogenics*, **22**: 3–16, 1982.
36. B. Turck, Effect of the respective position of filament bundles and stabilizing copper on coupling losses in superconducting composites, *Cryogenics*, **22**: 466–468, 1982.
37. A. Nijhuis *et al.*, Coupling loss time constant in full size Nb_3Sn CIC model conductors for fusion magnets, *Adv. Cryog. Eng. Mat.*, **42B**: 1281–1288, 1996.
38. H. Brechna G. Ries, Ac losses in superconducting synchrotron magnets, *IEEE Trans. Nucl. Sci.*, **18** (3): 639–642, 1971.
39. G. Ries, Ac losses in multifilamentary superconductors at technical frequencies, *IEEE Trans. Magn.* **13** (1): 524–527, 1977.
40. J. P. Soubeyrand B. Turck, Losses in superconducting composites under high rate, pulsed transverse field, *IEEE Trans. Magn.*, **15**: 248–251, 1979.
41. A. Nijhuis et al., Electromagnetic and mechanical characterization of ITER CS-MC conductors affected by transverse cyclic loading, part 1: Coupling currents loss, *IEEE Trans. Appl. Supercond.* **9**, 1063–1072, 1999.
42. A. M. Campbell, The effect of transport current and saturation on the losses of multifilamentary superconducting wires, *Cryogenics*, **21**: 107–112, 1981.
43. D. Ciazynski, Effect of the transport current on the losses of a superconducting composite under fast changing magnetic field, *IEEE Trans. Magn.*, **21**: 169–172, 1985.
44. P. Bruzzone et al., Test results for the high field conductor of the iter central solenoid model coil, *Adv. Cryog. Eng.*, **45**, to be published.
45. J. H. Murphy et al., Field orientation dependence of ac losses in rectangular multifilamentary superconductors, *Adv. Cryog. Eng.*, **22**: 420–427, 1975.
46. B. Turck et al., Coupling losses in a rectangular multifilamentary composite, *Cryogenics*, **22**: 441–450, 1982.
47. E. Seibt, Investigations of a steel reinforced NbTi superconducting flat cable for toroidal field magnets, *IEEE Trans. Magn.*, **15**: 804–807, 1979.
48. P. Bruzzone, Ac losses in high current superconductors for nuclear fusion magnets, Ph. D. Thesis, ETH 8224, Zurich, 1987.
49. G. Ries S. Takács, Coupling losses in finite length of superconducting cables and in long cables partially in magnetic field, *IEEE Trans. Magn.*, **17**: 2281–2284, 1981.
50. S. Takács, Coupling losses in cables and in spatially changing ac fields, *Cryogenics*, **22**: 661–665, 1982.

51. A. A. Akhmetov, A. Devred, T. Ogitsu, Periodicity of crossover currents in a Rutherford-type cables subjected to a time-dependent magnetic field, *J. Appl. Phys.*, **75**: 3176–3183, 1994.
52. L. Krempasky C. Schmidt, Theory of "supercurrents" and their influence on field quality and stability of superconducting magnets, *J. Appl. Phys.*, **78**: 5800–5810, 1995.
53. A. P. Verweij, Electrodynamic of superconducting cables in accelerator magnets, Ph.D. Thesis, Univ. of Twente, Enschede, The Netherlands 1995.
54. L. Krempasky C. Schmidt, Ramp rate limitation in large superconducting magnets due to "supercurrents," *Cryogenics*, **36**: 471–483, 1996.
55. P. Bruzzone, Ac losses and stability on large cable-in-conduit superconductors, *Phys. C*, **310**: 240–246, 1998.
56. A. Nijhuis, P. Bruzzone, H. H. J. ten Kate, Influence of Cr plating on the coupling loss in cable-in-conduit conductors, *Appl. Supercond. 1997, Inst. Phys. Conf.*, **158**: 921–924, 1997.
57. M. D. Sumption et al., Contact resistance and cable loss measurements of coated strands and cables wound from them, *IEEE Trans. Appl. Supercond.*, **5**: 692–695, 1995.
58. M. D. Sumption et al., Calorimetric measurements of the effect of nickel and Stabrite coatings and resistive cores on ac loss in accelerator cables under fixed pressure, *Adv. Cryog. Eng.*, **42**: 1303–1311, 1996.
59. E. W. Collings et al., Magnetic studies of ac loss in pressurized Rutherford cables with coated strands and resistive cores, *Adv. Cryog. Eng.*, **42**: 1225–1232, 1996.
60. D. Richter et al., Dc measurement of electrical contacts between strands in superconducting cables for the LHC main magnets, *IEEE Trans. Appl. Supercond.*, **7**: 786–789, 1997.
61. T. Hamajima et al., Ac loss performance of the 100 kWh SMES model coil, *Proc. of Magnet Technology Conf.*, **16**, Sept. 99, Ponte Vedra, FL.
62. A. Kawagoe et al., Increase of interstrand coupling losses of superconducting cable-in-conduit for acutal condition of sweep rate, *IEEE Trans. Appl. Supercond.* **9**: 727–730, 1999.
63. J. M. Depond et al., Examination of contacts between strands by electrical measurement and topographical analysis, *IEEE Trans. Appl. Supercond.*, **7**: 793–796, 1997.
64. T. M. Mower Y. Iwasa, Experimental investigation of ac losses in cabled superconductors, *Cryogenics*, **26**: 281–292, 1986.
65. K. Kwasnitza, A. Sultan, S. Al-Wakeel, Ac losses of a 10 kA NbTi cable-in-conduit superconductor for SMES application, *Cryogenics*, **36**: 27–34, 1996.
66. M. Nishi et al., Test results of the DPC-TJ, a 24 kA–40 A/mm^2 superconducting test coil for fusion machines, *Fusion technology 1992, Proc. 17th SOFT*, 1993, p. 912–916.
67. P. Bruzzone, A. Nijhuis, H. H. J. ten Kate, Effect of Cr plating on the coupling current loss in cable-in-conduit conductors, *Proc. ICMC 96*, Kitakyushu, Japan, May 1996, Amsterdam, The Netherlands Elsevier, p. 1243–1248.
68. Y. Ipatov, P. Dolgosheev, V. Sytnikov, Prospective barrier coatings for superconducting cables, *Supercond. Sci. Technol.*, **10**: 507–511, 1997.
69. A. Nijhuis et al., Parametric study on coupling loss in subsize ITER Nb_3Sn cabled specimen, *IEEE Trans. Magn.*, **32**: 2743–2746, 1996.
70. P. Bruzzone, A. Nijhuis, H. H. J. ten Kate, Contact resistance and coupling loss in cable-in-conduit of Cr plated Nb_3Sn strands, *Proc. MT-15*, Beijing, October 1997, Science Press, 1998, p. 1295–1298.
71. A. Nijhuis, H. H. J. ten Kate, P. Bruzzone, The influence of Lorentz forces on the ac loss in sub-size cable-in-conduit conductors for ITER, *IEEE Trans. Appl. Supercond.*, **7**: 262–265, 1997.
72. G. Ries, Stability in superconducting multistrand cables, *Cryogenics*, **20**: 513–519, 1980.
73. P. Bruzzone, Stability under transverse field pulse of the Nb_3Sn ITER cable-in-conduit conductor, *Proc. of Magnet Technology Conf.*, **16**, Sept. 1999, Ponte Vedre, FL.
74. P. Bruzzone et al., Coupling currents losses bench mark test of ITER subsize conductor, *IEEE Trans. Magn.*, **32**: 2826–2829, 1996.
75. L. Krempasky C. Schmidt, Time constant measurements in technical superconductors, *Cryogenics*, **39**: 23–33, 1999.

PIERLUIGI BRUZZONE
Centre de Recherches en Physique des Plasmas